

# Conservative cascade interpolation on the sphere: An intercomparison of various non-oscillatory reconstructions

Matthew R. Norman,<sup>a\*</sup> Fredrick H. M. Semazzi<sup>a</sup> and Ramachandran D. Nair<sup>b</sup>

<sup>a</sup>*Marine, Earth, & Atmospheric Sciences, North Carolina State University, USA*

<sup>b</sup>*National Center for Atmospheric Research, Boulder, CO, USA*

**ABSTRACT:** Various new polynomial and non-polynomial approximations to a subgrid distribution have been adapted for use in the conservative cascade scheme (CCS) and applied to conservative grid-to-grid interpolation on a latitude–longitude grid. These approximations include the following: piecewise parabolic method (PPM), piecewise hyperbolic method (PHM), piecewise double hyperbolic method (PDHM), power-limited piecewise parabolic method (P-PPM), piecewise rational method (PRM), third-order weighted essentially non-oscillatory (WENO23), fifth-order weighted essentially non-oscillatory (WENO35), and a modified piecewise parabolic method (M-PPM). A series of test cases are performed in which initial gridded data are interpolated between  $T42$  and  $2^\circ$  grids and compared against analytical values. Four initial data profiles are used: smooth harmonic, high-frequency harmonic, quasi-polar vortex data and slotted cylinder data. In general, PDHM (WENO35) had the lowest error norms of the three-(five-)cell stencil methods. Quite often, M-PPM gave accuracy comparable to WENO35 at significantly lower cost. Monotonicity violations generally only occurred when interpolating to a finer grid with a maximum violation of 1.8% of the data range. Copyright © 2009 Royal Meteorological Society

KEY WORDS non-oscillatory; conservative interpolation; conservative cascade scheme; WENO; spherical

Received 30 October 2008; Revised 9 February 2009; Accepted 11 February 2009

## 1. Introduction

Conservative remapping involves accurately transferring data from one grid to another while conserving the global and local integrals. Methods currently existing in the literature for meteorological application include those of Jones (1999), Lauritzen and Nair (2008) and Ulrich *et al.* (2009). The basic conservative interpolation steps of Nair *et al.* (2002) and Zerroukat *et al.* (2004) can also be used for geophysical interpolation. The method of Jones (1999) is very flexible and is applicable to many spherical grids. However, it is at most second-order accurate. Nair *et al.* (2002) and Zerroukat *et al.* (2004) employ a conservative cascade interpolation to calculate mass in departure cells for semi-Lagrangian advection on the sphere. Lauritzen and Nair (2008) apply the conservative cascade methodology for interpolation between regular latitude–longitude (RLL) grids and cubed-sphere grids. Ulrich *et al.* (2009) developed a novel fully two-dimensional approach to remapping between cubed-sphere and RLL grids, which exactly integrates polynomial reconstructions via quadrature on cell boundaries. The primary focus of this study is on the relative performance of various one-dimensional non-oscillatory reconstructions, many of which have had little exposure to meteorological application. To this end, we choose the conservative cascade scheme (CCS) of Nair *et al.* (2002) and Norman

and Nair (2008) as a framework testbed for this inter-comparison.

Nair *et al.* (2002) and Norman and Nair (2008) applied the CCS to semi-Lagrangian (SL) transport on a RLL grid. Cascade interpolation is more efficient than a straightforward Cartesian splitting and involves fewer operations, especially for multiple species, since the intermediate grid needs to be generated only once (Purser and Leslie, 1991; Nair *et al.*, 1999). The CCS also applies unchanged to the more general realm of geophysical grid-to-grid interpolation, which has different computational challenges from SL transport. In the transport case, the scheme must be robust enough to handle a wide range of target grids as the wind flow varies in time. This is a notable difference from conservative interpolation, in which the source and target grids are typically static. Also, for SL transport there must exist an equal number of source and target grid cells. This means that the size of source and target grid cells on average are similar. In conservative interpolation there is no such restriction. There may be multiple target cells within every source cell and vice versa. In this study, the CCS is being applied to one step of conservative interpolation between two regular latitude–longitude grids. As in the transport case, non-oscillatory reconstructions during each one-dimensional (1-D) CCS sweep ensure that the violation of monotonicity during the remapping is well controlled. Other techniques of conservative cascade remapping do exist, such as in Zerroukat *et al.* (2004).

\*Correspondence to: Matthew R. Norman, Box 8208 NCSU Campus, Raleigh, NC 27695, USA. E-mail: mnorman@ncsu.edu

There are many applications of grid-to-grid interpolation in geophysical numerical simulation. For instance, the initial conditions and boundary conditions are always interpolated from data sets onto the model grid. Also, most components of an Earth system model are simulated on different grids, and when coupled interpolation between those grids is necessary. In adaptive mesh refinement (AMR), the grids are locally refined and coarsened, requiring interpolation between grids. Nothing precludes application to the restriction and prolongation operations in multigrid either, for that matter. Also, as mentioned earlier, SL transport utilizes an interpolation step in remapping mass from the static grid to the departure grid.

One general rule applies to all of these applications: the properties of the interpolation will propagate through the simulation. For example, a numerical weather prediction (NWP) forecast is forced mostly by initial conditions. Thus, if the initial conditions are inaccurately interpolated to the model grid, even high-order dynamical solvers will render inaccurate forecasts. The same can be said about climate simulations, which are almost entirely boundary-value problems owing to their very long simulation times. With such high sensitivity to boundary specifications, a low-order accurate interpolation should not be coupled with high-order accurate dynamics. If the interpolation used when coupling two components is not conservative, the overall simulation will not be conservative. If the interpolation used in AMR grid refinement is oscillatory, the simulation will exhibit oscillations. Therefore, if certain properties are desirable in a dynamical simulation, those same properties must be true of the interpolations used to transfer data from grid to grid.

The purpose of the present study is to perform an intercomparison of various functional approximations in the CCS applied to conservative interpolation between two latitude–longitude grids. These approximations include the piecewise parabolic method (PPM) and non-polynomial approximations from Norman and Nair (2008) as well as four new polynomial functions. The new reconstructions are the power-limited piecewise parabolic method (P-PPM), third-order weighted essentially non-oscillatory (WENO23) method, fifth-order weighted essentially non-oscillatory (WENO35) method, and a modified PPM (M-PPM). The M-PPM, developed in this study, uses a convex combination of the original full-order reconstruction and the classical limited reconstruction with the weighting defined by a mathematical indicator of jump discontinuity severity in the stencil.

There exist other polynomial interpolants in literature not included in this article. For instance, Zerroukat *et al.* (2004) and Zerroukat *et al.* (2006) used piecewise cubic polynomials and quadratic splines, respectively, and both are limited by the filter provided in Zerroukat *et al.* (2005). These reconstructions are accurate, but cubics along with their filter require a wide stencil, and the splines require a global stencil. Small-stencil methods give an advantage in regard to scalability in that communication demand in parallel architectures is reduced compared with wide-stencil and global-stencil

methods. Additionally, smaller stencil methods can be used closer to a material boundary (e.g. the Earth's surface) than wider stencil methods. For this reason, we wish to restrict our attention to small-stencil methods, meaning the reconstruction of a cell requires a stencil of 5 cells or less (including the cell in question). Also, Blossey and Durran (2008) introduced a PPM variant wherein the classical limiter is only employed when a WENO-like parameter exceeds a certain threshold, indicating a sufficiently large discontinuity. In fact, the M-PPM method developed in section 2.3 carries a similar approach: only limit the reconstruction to the degree to which it has the potential to cause oscillations.

The article is organized as follows. Section 2 describes the subgrid reconstructions, section 3 describes the test cases for the study, section 4 presents the numerical results, and conclusions are drawn in section 5.

## 2. Subgrid reconstructions

### 2.1. Non-polynomial reconstructions

For sake of brevity, the details of the non-polynomial reconstructions will not be reviewed in the present article because they are implemented as described in Norman and Nair (2008), which describes them in detail. These reconstructions include the piecewise hyperbolic method (PHM) of Marquina (1994) and Serna (2006), the piecewise double hyperbolic method (PDHM) of Artebrant and Schroll (2006) and the piecewise rational method (PRM) of Xiao *et al.* (2002). For the reader's convenience, all functional approximations and their acronyms are defined in Table I along with the stencil required for each method. PHM and PDHM are implemented exactly as given in Serna (2006) and Artebrant and Schroll (2006), respectively. Additionally, PRM is implemented in this context

Table I. Functional approximations of this study, their respective acronyms and the stencil size required. Here, the stencil is defined as the total number of cells of information required for reconstruction of one cell (including the cell being reconstructed).

Acronym	Functional approximation	Stencil
PPM	Classical piecewise parabolic method	5
P-PPM	Power-limited piecewise parabolic method	3
WENO23	Third-order weighted essentially non-oscillatory	3
WENO35	Fifth-order weighted essentially non-oscillatory	5
PHM	Piecewise hyperbolic method	3
PDHM	Piecewise double hyperbolic method	3
PRM	Piecewise rational method	5
M-PPM	Modified piecewise parabolic method	5

with the same functional form as given in Xiao *et al.* (2002) with fourth-order accurate interface values following the PPM of Colella and Woodward (1984).

2.2. Power-limited piecewise parabolic method (P-PPM)

The idea behind P-PPM is given in Amat *et al.* (2003), hereafter ABC03. The classical PPM of Colella and Woodward (1984), which serves as a basis of comparison for the other reconstructions of this study, uses the cell mean and fourth-order approximation to the left and right cell boundary values. The ABC03 parabolic formulation uses the cell mean and second-order estimates of the left and right derivatives in a manner very similar to the PHM of Marquina (1994). Consider an arbitrary cell,  $I_i$ , defined on the interval  $[x_{i-1/2}, x_{i+1/2}]$  with geometric centre  $x_i$  and a grid spacing of  $\Delta x_i = x_{i+1/2} - x_{i-1/2}$  with a cell mean of  $\bar{u}_i$ ; that is

$$\bar{u}_i \Delta x_i = \int_{x_{i-1/2}}^{x_{i+1/2}} u(x) dx.$$

The following three relations constrain a unique parabola,  $r_i(x)$ , defined on cell  $I_i$ :

$$\int_{x_{i-1/2}}^{x_{i+1/2}} r_i(x) dx = \bar{u}_i \Delta x_i,$$

$$r'_i(x_i) = d_C,$$

$$\begin{cases} r'_i(x_{i-1/2}) = d_L & \text{if } |d_L| \leq |d_R| \\ & \text{or} \\ r'_i(x_{i+1/2}) = d_R & \text{otherwise.} \end{cases}$$

The parameters  $d_L$ ,  $d_R$ , and  $d_C$  represent second-order approximations to the left, right, and centred derivatives, respectively.

ABC03 chose a polynomial of the global form  $r_i(x) = a_{0,i} + a_{1,i}x + a_{2,i}x^2$ , but here a local formulation is used instead:

$$r_i(x) = a_{0,i} + a_{1,i}(x - x_i) + a_{2,i}(x - x_i)^2.$$

The coefficients are thus defined as

$$\begin{cases} a_{2,i} \Delta x_i = d_C - d_L & \text{if } |d_L| \leq |d_R| \\ & \text{or} \\ a_{2,i} \Delta x_i = d_R - d_C & \text{otherwise,} \end{cases}$$

$$a_{1,i} = d_C,$$

$$a_{0,i} = \bar{u}_i - a_{2,i} \frac{\Delta x_i^2}{12}.$$

Note that the lateral derivatives,  $d_L$  and  $d_R$  must be second-order to achieve third-order reconstruction for sufficiently smooth fields. For unequal grid spacing, the most straightforward approach to second-order derivative estimates is to reconstruct a third-order accurate parabola,

$P_3(x)$ , across the three-cell stencil,  $I_{i-1} \cup I_i \cup I_{i+1}$  (the primitive of which matches the cell means), and differentiate it at the left and right cell boundary locations:  $d_L = P'_3(x_{i-1/2})$  and  $d_R = P'_3(x_{i+1/2})$ . This polynomial  $P_3(x)$  is identical to  $P_{\text{EXACT}}(x)$  in Appendix A. Additionally, for any method that uses second-order lateral derivative approximations for reconstruction (e.g. PHM and PDHM), this is how those derivatives are computed in the meridional direction.

Now, the centred derivative estimate,  $d_C$ , is all that is left to calculate. This estimate is what acts to limit the local total variation (LTV) of the parabola to achieve an essentially non-oscillatory reconstruction. A naive choice would be the simple arithmetic mean,  $d_C = (d_L + d_R) / 2$ , but this does not bound the LTV. ABC03 used instead the harmonic mean of Marquina (1994):

$$d_C = \text{mins}(d_L, d_R) \frac{2|d_L||d_R|}{|d_L| + |d_R| + \epsilon},$$

where  $\epsilon$  is a machine-precision number used to avoid a floating point divide-by-zero and

$$\begin{cases} \text{mins}(d_L, d_R) = \text{sign}(d_L) & \text{if } |d_L| \leq |d_R| \\ & \text{or} \\ \text{mins}(d_L, d_R) = \text{sign}(d_R) & \text{otherwise.} \end{cases}$$

This provided a satisfactorily limited parabola. More recently, however, a generalized mean, Powereno $_p$ , (Serna and Marquina, 2004; Serna, 2006) has been developed defining the centred derivative as a power-limited mean of the lateral derivatives given by

$$d_C = \text{mins}(d_L, d_R) \frac{|d_L| + |d_R|}{2} \times \left( 1 - \left| \frac{|d_L| - |d_R|}{|d_L| + |d_R| + \epsilon} \right|^p \right), \quad (1)$$

where  $p$  is a parameter controlling the local variation of the reconstruction. It was shown in Serna and Marquina (2004) that increasing  $p$  acts to increase the LTV of hyperbolae asymptotically to that of using an arithmetic mean as  $p \rightarrow \infty$ , and the same is true for parabolae. Therefore, we adopt the power limiter instead of the ABC03 harmonic limiter in this study, with  $p = 4$  to allow more local variation while still keeping the parabolae limited.

2.3. Modified piecewise parabolic method (M-PPM)

It is well known that the original PPM limiter of Colella and Woodward (1984) degrades the reconstruction to first-order accuracy at all extrema in order to preserve monotonicity. Recently, a modified limiter for PPM was developed in Colella and Sekora (2008) for uniform grid spacing. This limiter gives improved accuracy at extrema via a non-oscillatory (not strictly monotonic) limiting based on second derivative information. However, the extension of this limiter to a non-uniform grid spacing is not trivial.

Therefore, here we present a new and different approach to improved PPM accuracy at extrema, wherein smooth extrema are reconstructed at full accuracy and non-smooth extrema are limited to avoid spurious oscillations. To indicate mathematically the presence of a jump discontinuity at either the left or the right cell boundary, we define a ‘jump severity indicator’,  $S$ , identical to the exponentiated term in Equation (1):

$$S = \left| \frac{|d_L| - |d_R|}{|d_L| + |d_R| + \epsilon} \right|. \quad (2)$$

Taking a geometric approach, if the *magnitude* of the first derivative changes very abruptly across a cell, that is a solid indicator of a jump discontinuity at which reconstructions tend to oscillate most. This indicator in essence gives an estimate of the second derivative magnitude confined to the normalized domain:  $S \in [0, 1]$ .  $S = 1$  indicates a strong jump discontinuity, and  $S = 0$  indicates a very smooth function.

We want to reconstruct at full accuracy for smooth extrema and at first-order accuracy for non-smooth extrema. Consider the classically limited left and right interface values,  $u_{\text{lim}}^-$  and  $u_{\text{lim}}^+$ , respectively. Also consider the left and right original interpolated interface values,  $u_{\text{orig}}^-$  and  $u_{\text{orig}}^+$ , respectively. We thus, define the left and right interface values used in the final interpolation,  $u_*^-$  and  $u_*^+$ , respectively as follows:

$$u_*^\pm = C_S u_{\text{lim}}^\pm + (1 - C_S) u_{\text{orig}}^\pm, \quad (3)$$

where  $C_S$  is any functional mapping of  $S$  to the same domain:  $C_S \in [0, 1]$ , with  $C_S = 0$  indicating a strong jump discontinuity and  $C_S = 1$  indicating smooth data (the reverse of  $S$  itself). The purpose of  $C_S$  is to control the variation of the reconstruction by specifying the sensitivity of the limiting to the value of the severity indicator,  $S$ . For example, the Serna (2006) hyperbolae use the mapping  $C_S(S) = 1 - S^3$  (i.e. the Powereno<sub>3</sub> limiter), proving that it allows more variation than the Marquina (1994) hyperbolae, which use the formal equivalent of the mapping  $C_S(S) = 1 - S^2$ . We found that much higher values of  $p$  can be used for this reconstruction for most cases. However, in the most severe of jumps ( $S \approx 1$ ) we found the need for a more conservative mapping. Therefore, we used the following mapping for our study to obtain accuracy when possible and limit oscillations in the severe cases:

$$C_S(S) = \begin{cases} 1 - S^6 & \text{if } S \leq 0.9, \\ 1 - S^3 & \text{if } S > 0.9. \end{cases}$$

There are two cases in which the parabolae of Colella and Woodward (1984) are limited. The first case (which has already been discussed above) is in the presence of extrema (i.e.  $(u_{\text{orig}}^+ - \bar{u})(\bar{u} - u_{\text{orig}}^-) < 0$ ). The second case is when the data itself are monotonic but the reconstructed parabola is not monotonic within the cell domain. Colella and Sekora (2008) note that the requirement of

fully monotonic parabolae within each cell domain in Colella and Woodward (1984) is sufficient but not necessary in order to obtain a monotonic reconstruction. In other words, the original limiting is more restrictive than formally necessary for monotonicity. The convex combination in Equation (3) need not be restricted to extrema alone but can be used (and is used in this study) for *all* cases in which the original parabola is being limited to provide less restrictive non-oscillatory parabolae.

The last modification of the classical PPM is to change the original calculation of interface values. Colella and Woodward (1984) calculated fourth-order accurate monotonic estimates of the interface values over the grid first and then used those for cell reconstruction in a second loop. Colella and Sekora (2008) revised the interface values to be sixth-order accurate, of course, using a six-cell stencil for each interface. These schemes calculate continuous interface values in one loop and then reconstruct the cells in another loop using those values. Our scheme, on the other hand, calculates both the interface values and the reconstruction in the same loop, rendering two discontinuous values for each interface even without limiting. A comparison in terms of CPU times will later show that this is only a slight overhead in terms of compute time.

We utilize the full five-cell stencil to reconstruct a polynomial and then sample it at the cell interfaces. We cannot always use a fifth-order accurate reconstruction, however, because if there exists a discontinuity in the left-most or rightmost cell, the polynomial will oscillate. Given that the limiting based on Equation (2) only takes into account a three-cell stencil, this could lead to uncontrolled oscillations. Therefore, we calculate jump severity indicators from Equation (2) for the cells to the left and right of the centre cell ( $S_L$  and  $S_R$ , respectively). If  $S_L$  or  $S_R$  exceed a threshold,  $S^*$ , there may be a discontinuity outside the centred three-cell stencil. Therefore, we adapt the stencil of the polynomial to remove any discontinuity that may lie in the leftmost or rightmost cell. This is described in more detail in Appendix B. A threshold value of  $S^* = 0.8$  was experimentally determined and used. The interface values are not limited to be monotonic. Rather, they are subjected to the same constraint given in Equation (3), where, in this case,  $u_{\text{orig}}^\pm$  and  $u_{\text{lim}}^\pm$  represent the the sampled polynomial values and the monotonically limited values respectively.

The only modifications to the original PPM of Colella and Woodward (1984) are in the calculation and limiting of interface values. The following steps summarize the process that is performed for each cell to complete the reconstruction.

- (1) Calculate the severity indicator defined by Equation (2).
- (2) Construct a polynomial across a five-cell stencil using the method described in Appendix B.
- (3) Sample the polynomial at the left and right cell boundaries to obtain fifth-order accurate interface values.

- (4) Calculate monotonically limited estimates of these interface values that are restricted to the range of the neighbouring cell means.
- (5) Calculate a convex combination of the interface values from step 3,  $u_{\text{orig}}^{\pm}$ , and the monotonic values from step 4,  $u_{\text{lim}}^{\pm}$ , using Equation (3).
- (6) Following Colella and Woodward (1984), determine whether this cell contains a local extremum or whether the parabola constructed from the left and right interface values and cell mean is non-monotonic. If so, calculate the limited value.
- (7) Calculate a convex combination of the interface values from step 5,  $u_{\text{orig}}^{\pm}$ , and the monotonically limited values from step 6,  $u_{\text{lim}}^{\pm}$ , again using Equation (3).
- (8) Using the interface values from step 7 and the cell mean, construct a parabola following Colella and Woodward (1984).

This modification of PPM (which we will denote M-PPM) is not strictly monotonic like PPM but is non-oscillatory like the other methods in this article. The M-PPM approach here is similar to that of Blossey and Durran (2008) in the sense that the original PPM limiter is only used for parabolae deemed oscillatory by a given formulaic indicator of non-smoothness. There is one main difference, however. The present work uses a functional mapping of the severity indicator to give a convex combination of the limited and unlimited solutions, and Blossey and Durran (2008) used a thresholding technique to determine if parabolae should be limited. This difference is similar in nature to the difference between ENO and WENO schemes (Harten *et al.*, 1987; Liu *et al.*, 1994).

To show a visual perspective of the effects of the M-PPM modifications in practice, Figure 1 shows a zoomed plot of a 1-D irregular signal profile (the same as in Norman and Nair, 2008) along with the PPM reconstruction, M-PPM reconstruction and the analytical profile. In the plot, we have an unresolved gradient

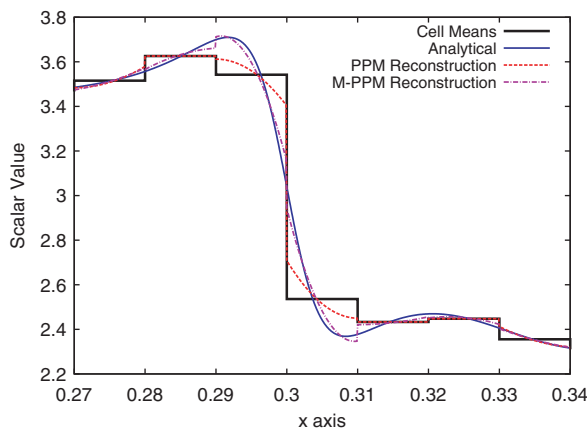


Figure 1. A prescribed irregular signal profile comparing the PPM and the M-PPM reconstructions. This figure is available in colour online at [www.interscience.wiley.com/journal/qj](http://www.interscience.wiley.com/journal/qj)

and a local maximum in the data to show the relative advantages.

#### 2.4. Weighted essentially non-oscillatory methods (WENO23 and WENO35)

This form of non-oscillatory approximation originates from articles such as Harten *et al.* (1987), Shu and Osher (1988), and Liu *et al.* (1994). The basic idea is as follows. First, create multiple polynomial approximations within different stencils, all of which must include the domain of the target reconstruction cell. Next, estimate the smoothness of each of the polynomials with a formula similar to total variation but for both first and second derivatives. Finally, compute weights based on the smoothness indicators such that the smoother polynomials are weighted more than the non-smooth polynomials. A detailed discussion of the WENO reconstruction philosophy is given in Shu (1999).

First, we will discuss WENO23, which is second-order accurate in the worst case and third-order accurate in the best case. The particular implementation used in this study is very similar to that of Kurganov and Levy (2000). The only difference is that here the grid spacing is not uniform in the meridional direction on the  $(\lambda, \mu)$  grid (Nair and Machenhauer, 2002). Therefore, the polynomials themselves and the smoothness indicators must be re-derived with this in mind, as given in Appendix A. The parameter,  $p$ , in Kurganov and Levy (2000) is set to  $p = 1/2$  and is found to bound the total variation satisfactorily. A lower value of  $p$  essentially allows more variation in the WENO23 reconstruction and converges more quickly to the optimal accuracy as data smoothness increases.

The WENO35 method, which is third-order accurate in the worst case and fifth-order accurate in the best case, is derived using similar principles to the WENO23 method. Four polynomials are defined: one fourth-order polynomial defined across a five-cell stencil centred about the target reconstruction cell, one second-order polynomial defined on the leftmost three cells, one second-order polynomial defined on the centred three cells, and one second-order polynomial defined on the rightmost three cells. Then the smoothness of each polynomial is evaluated with a total variation estimate applied to all existing derivatives in the approximations. Next, the weights are formed based on the smoothness indicators, with the smoothest functions weighted the most. Finally, the weights yield a convex combination of the four polynomials to yield a final reconstruction that is non-oscillatory near discontinuities yet fifth-order accurate in the presence of smooth data. This implementation is fully described in detail in the reconstruction section of Capdeville (2008). The only way the present implementation differs is in the calculation of the weights. After calculating the smoothness indicators,  $IS_j$ , Capdeville (2008) creates weights defined by  $w_j = (\epsilon + IS_j)^{-2}$ . We use a similar approach to Kurganov and Levy (2000) and define them as  $w_j = (\epsilon + IS_j)^{-p}$  using  $p = 1/2$ .

It is worth noting that the accuracy of WENO23 and WENO35 is strongly dependent upon the value of  $p$ , which controls how quickly the reconstruction converges to full-order accuracy as the smoothness indicators converge to equal values. The value of  $p = 1/2$  is used here instead of the standard  $p = 2$  because it seems to render much better accuracy while still controlling the violation of monotonicity to a sufficiently small magnitude (1–2% in the worst cases).

We found through experimentation that if a particularly strong jump discontinuity exists in the centre cell, all four WENO35 polynomial interpolants will oscillate strongly. This can cause relative overshoot magnitudes of 10–20% in the CCS context, which is highly unacceptable in a non-oscillatory scheme. This is much less severe in the WENO23 scheme as the polynomial orders are lower. To mitigate this effect we experimentally determined the jump severity indicators at which WENO35 oscillates unacceptably and use WENO23 instead in a hybrid fashion. We found that if we use WENO23 instead of WENO35 for  $S > 0.98$ , the oscillations are much better controlled without greatly affecting the accuracy of the overall WENO35 method. The calculation of  $S$  is very cheap, so there is no measurable computational overhead associated with this modification.

### 3. Test cases

Four types of global spherical data are used for test cases in this study, three of them adopted from Lauritzen and Nair (2008). The first two test data sets are originally from Jones (1999), giving one smooth and one high frequency harmonic function. The smooth function denoted  $Y_2^2$  and the high-frequency function denoted  $Y_{32}^{16}$  are defined as

$$Y_2^2 = 2 + \cos^2 \theta' \cos(2\lambda')$$

$$Y_{32}^{16} = 2 + \sin^{16}(2\theta') \cos(16\lambda'),$$

where  $(\lambda', \theta')$  are the coordinates on a sphere that is rotated relative to the true sphere. This rotation is a feature provided to avoid symmetry on the grid and place the data in locations (typically the poles) that reveal errors on the grid. Both the  $Y_2^2$  data and the  $Y_{32}^{16}$  data have the rotated sphere's pole located at  $0^\circ$  longitude and  $45^\circ$  latitude on the true sphere. These are shown in Figure 2(a) and (b). Note that the  $45^\circ$  latitude rotation places the  $Y_{32}^{16}$  high frequency belt passing through the poles. The third test case data set produces a vortex at both poles of a rotated sphere. It is defined exactly as in Lauritzen and Nair (2008), with the poles of the rotated sphere located at  $0^\circ$  longitude and  $81^\circ$  latitude. The vortex data are shown in Figure 2(c).

The fourth test case implements a slotted cylinder on the sphere located at the equator. The slotted cylinder originates from Zalesak (1979) and was implemented on the sphere by Nair *et al.* (2003). It is intended to test a scheme's behaviour in the presence of a

multidimensional data jump discontinuity. First, a radius is specified in terms of the rotated latitude and longitude:

$R = \sqrt{(\lambda')^2 + (\theta')^2}$ . Then the analytical profile is as follows:

$$Y = \begin{cases} 0 & \text{if } R > \frac{10\pi}{64}, \\ 0 & \text{if } R \leq \frac{10\pi}{64} \text{ and } |\lambda'| < \frac{10\pi}{192} \text{ and } \theta' > -\frac{10\pi}{192}, \\ 1 & \text{otherwise.} \end{cases}$$

Quadrature is not used for this test case because we want the profile to be as sharp as possible. Thus, cell centroid values are used to make sure there is a discontinuous jump from zero to unity. For this reason, the only error norms that are valid are the  $L_{\min}$  and  $L_{\max}$  norms (which manifest oscillations) because we know the data range is always between zero and unity.

Each of the seven subgrid approximations is tested for intercomparison with the following standard global error norms:  $L_1$ ,  $L_2$ ,  $L_\infty$ ,  $L_{\min}$  and  $L_{\max}$ . The formulae are given in Lauritzen and Nair (2008). To briefly discuss the properties of the different error measures,  $L_1$  expresses the most straightforward error measure giving the mean absolute error normalized by the average magnitude of the exact data.  $L_\infty$  expresses the largest magnitude of error on the grid normalized by the largest magnitude of the exact data. Most notably for  $L_{\min}$ , a negative value indicates violation of positivity. Both  $L_{\min}$  and  $L_{\max}$  are normalized by the range of the exact data.  $L_2$ , closely related to the root-mean-square error, is the 2-norm of the absolute error normalized by the 2-norm of the exact data, rendering a larger weighting for larger errors.

For all four data profiles and all eight approximations, two conservative interpolations will be performed for intercomparison. First, the data will be interpolated from a  $2^\circ$  grid to a  $T42$  grid ( $\approx 2.8^\circ$  grid spacing) to test the accuracy and oscillatory properties in a coarsening interpolation. Then, the reverse will be performed to test the same properties in a sharpening interpolation. To avoid the need to integrate these complex functions analytically in even more complex rotated coordinates, a five-point Gaussian quadrature is used to obtain cell mean estimates of an order much higher than the order of interpolation, thus retaining a meaningful error measure for intercomparison.

### 4. Numerical results

PPM will serve as a baseline for comparison, due to its general acceptance and use in the atmospheric modelling community. No positive definite filter is used in this study for the purpose of observing the natural potential of each function to violate positivity.

For the reader's convenience, a comparative bar chart of  $L_1$  error is given in Figure 3 to get a quick overall perspective of accuracy.

Considering the very smooth harmonic data,  $Y_2^2$  (Table II) in a coarsening interpolation, the only methods performing worse than PPM are PRM and WENO23 by a slight margin. It appears from the  $L_{\min}$  and  $L_{\max}$  norms that PPM is experiencing undershoots and overshoots. However, this is not because PPM is not monotonic but because the  $2^\circ$  exact cell means have a larger range than the  $T42$  exact cell means due to the higher resolution of the analytical function. In particular, the  $L_\infty$  norm for M-PPM shows that it is resolving the smooth extrema

much better than the other methods. In the sharpening interpolation for these same data, as expected, the error norms are larger. The most notable result is that PDHM easily stands out as the most accurate interpolant by an order of magnitude. The advantages of M-PPM are much less pronounced in the sharpening interpolation.

Moving on to the less smooth harmonic data,  $Y_{32}^{16}$  (Table III), in the coarsening interpolation, we see violations of positivity of the order of 0.1% many of which, again, are due to the higher resolution of extrema in

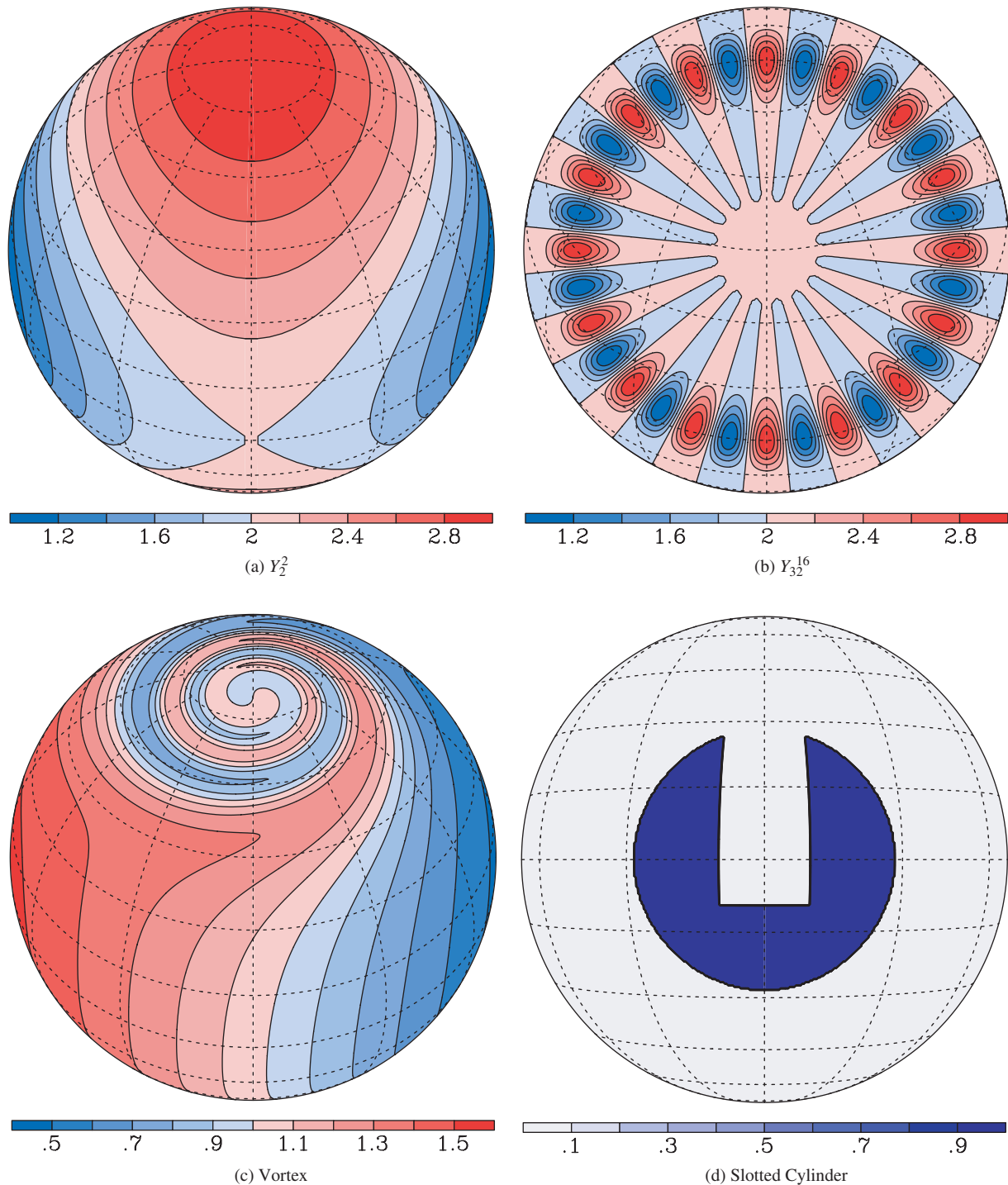


Figure 2. Analytical plots of the three data profiles used in this study. (a)  $Y_2^2$ , (b)  $Y_{32}^{16}$ , (c) vortex, (d) slotted cylinder. This figure is available in colour online at [www.interscience.wiley.com/journal/qj](http://www.interscience.wiley.com/journal/qj)

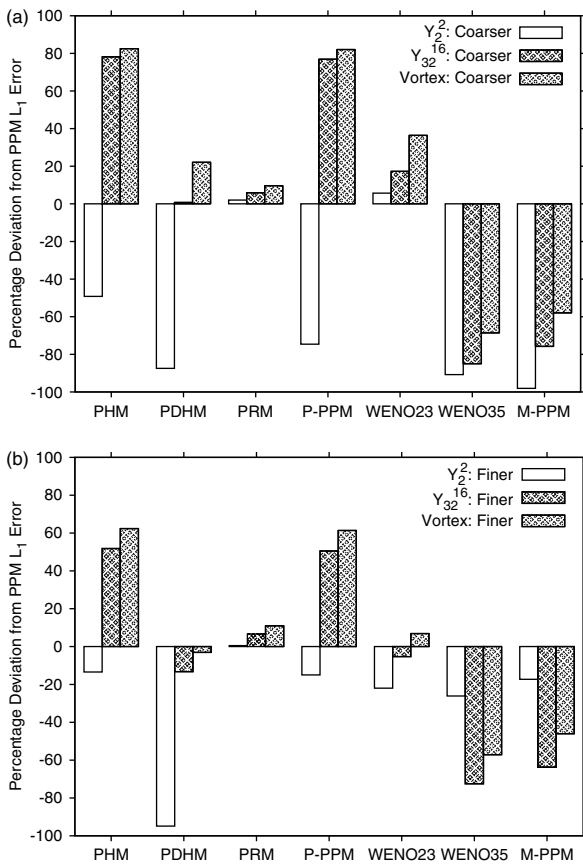


Figure 3. Percentage deviation of  $L_1$  error from PPM for the  $Y_2^2$ ,  $Y_{32}^{16}$  and vortex test cases. (a) Coarsening interpolations, (b) sharpening interpolations. ‘Coarser’ denotes an interpolation from a  $2^\circ$  grid to a  $T42$  grid and ‘Finer’ denotes the reverse.

the exact  $2^\circ$  data profile. Here, M-PPM and WENO35 separate themselves as the most accurate reconstructions for a non-smooth function with a large number of spurious extrema. Most notable is the improvement in the  $L_\infty$  norm for M-PPM, evidencing better resolution of the sharp extrema. For the sharpening interpolation, we have violations of positivity of the order of 1% (1.6% max), and only PHM and P-PPM violated monotonicity in this case. Once again, WENO35 and M-PPM separate themselves as the most accurate reconstructions.

The vortex data test case (Table IV) for the coarsening interpolation shows little in the way of monotonicity violation. WENO35 and M-PPM have the lowest error norms. As typically seems to be the case, PRM is similar

to PPM but slightly less accurate. This is likely because they use the same interface values. In the sharpening case, there are no violations of monotonicity manifested by the error norms. Like the coarsening interpolation, WENO35 and M-PPM perform the best with M-PPM slightly less accurate overall.

As mentioned in section 3, the slotted cylinder test case is intended to challenge the ability of a reconstruction to control oscillations with strong jump discontinuities. The magnitudes of these oscillations are manifested in the  $L_{\min}$  and  $L_{\max}$  norms. For both the coarsening and sharpening interpolations, the oscillation magnitudes for all of the methods were of order 1% or less. The worst violation occurred with M-PPM, which had an undershoot of 1.8% in the sharpening interpolation. To give a frame of reference for this test case, when using only the optimal polynomial of WENO35 an overshoot of 32% occurred.

Accuracy alone does not determine efficiency but also run time and scalability, the most straightforward of which is run time. To consider this, Table V lists the run times of each of the methods for the vortex test case interpolating from a  $1/3^\circ$  grid ( $1080 \times 540$ ) to a  $1/2.5^\circ$  grid ( $900 \times 450$ ). The codes have been optimized, avoiding exponentiation whenever possible and replacing repeated operations with precomputed variables. Clearly, PRM and P-PPM separate themselves as the cheapest reconstructions in terms of speed. WENO35 is clearly more expensive than any of the other methods, yet it also tends to give the best accuracy. It is possible that the run time may be improved via vectorization for both WENO35 and WENO23, as they make use of several matrix–vector products during the reconstruction. M-PPM actually requires about 7% more computation than PPM while typically giving much greater accuracy using the same stencil.

Now, regarding scalability the three-cell methods have the potential to scale more efficiently to a larger number of processors than do the five-cell methods, due to a reduced communication burden per remapping. As shown in Table I, PHM, PDHM, P-PPM and WENO23 are the three-cell stencil methods (requiring a one-cell halo when parallelized), and PPM, M-PPM, PRM and WENO35 are the five-cell stencil methods (requiring a two-cell halo when parallelized).

Table II. Error norms for the  $Y_2^2$  test case.

	$2^\circ$ interpolated to $T42$					$T42$ interpolated to $2^\circ$				
	$L_1$	$L_2$	$L_\infty$	$L_{\min}$	$L_{\max}$	$L_1$	$L_2$	$L_\infty$	$L_{\min}$	$L_{\max}$
PPM	2.46E-06	6.14E-06	6.25E-05	-3.09E-05	4.69E-05	3.87E-05	1.01E-04	4.75E-04	5.95E-04	-2.98E-04
PHM	1.25E-06	2.14E-06	8.47E-06	9.61E-06	-2.39E-07	3.35E-05	8.70E-05	3.97E-04	5.95E-04	-2.98E-04
PDHM	3.08E-07	3.93E-07	7.55E-07	4.78E-07	0.00E+00	1.98E-06	1.25E-05	3.92E-04	3.22E-06	-2.75E-04
PRM	2.51E-06	5.97E-06	5.81E-05	-2.96E-05	4.37E-05	3.89E-05	9.99E-05	4.72E-04	5.95E-04	-2.98E-04
P-PPM	6.25E-07	9.73E-07	3.70E-06	5.55E-06	0.00E+00	3.29E-05	8.80E-05	3.97E-04	5.95E-04	-2.98E-04
WENO23	2.60E-06	4.71E-06	2.08E-05	3.12E-05	0.00E+00	3.02E-05	7.34E-05	3.79E-04	5.43E-04	-2.74E-04
WENO35	2.27E-07	3.54E-06	7.88E-05	0.00E+00	5.92E-05	2.86E-05	8.27E-05	3.79E-04	5.43E-04	-2.74E-04
M-PPM	4.75E-08	6.74E-08	1.19E-07	0.00E+00	0.00E+00	3.20E-05	8.96E-05	3.97E-04	5.95E-04	2.46E-06

Table III. Error norms for the  $Y_{32}^{16}$  test case.

	$2^\circ$ interpolated to $T42$					$T42$ interpolated to $2^\circ$				
	$L_1$	$L_2$	$L_\infty$	$L_{\min}$	$L_{\max}$	$L_1$	$L_2$	$L_\infty$	$L_{\min}$	$L_{\max}$
PPM	7.80E-04	2.06E-03	1.27E-02	1.19E-02	1.56E-03	3.78E-03	9.37E-03	4.99E-02	2.59E-02	-9.47E-03
PHM	1.39E-03	3.45E-03	1.50E-02	1.38E-02	1.89E-05	5.74E-03	1.37E-02	5.49E-02	6.39E-03	1.56E-02
PDHM	7.86E-04	2.02E-03	1.38E-02	1.37E-02	1.44E-05	3.28E-03	8.24E-03	5.42E-02	2.24E-02	-9.42E-03
PRM	8.26E-04	2.15E-03	1.30E-02	1.08E-02	1.40E-03	4.03E-03	9.84E-03	5.04E-02	9.84E-03	-6.37E-03
P-PPM	1.38E-03	3.45E-03	1.50E-02	1.33E-02	1.41E-05	5.69E-03	1.37E-02	5.50E-02	5.72E-03	1.64E-02
WENO23	9.15E-04	2.27E-03	1.28E-02	1.42E-02	-1.09E-05	3.58E-03	8.73E-03	4.89E-02	2.78E-02	-9.40E-03
WENO35	1.17E-04	4.84E-04	1.01E-02	7.00E-05	1.99E-03	1.04E-03	3.92E-03	4.59E-02	1.55E-03	-8.21E-03
M-PPM	1.89E-04	6.65E-04	7.31E-03	1.74E-03	3.37E-06	1.37E-03	4.52E-03	4.56E-02	3.45E-03	-9.45E-03

Table IV. Error norms for the vortex test case.

	$2^\circ$ interpolated to $T42$					$T42$ interpolated to $2^\circ$				
	$L_1$	$L_2$	$L_\infty$	$L_{\min}$	$L_{\max}$	$L_1$	$L_2$	$L_\infty$	$L_{\min}$	$L_{\max}$
PPM	2.17E-04	9.48E-04	1.00E-02	-3.28E-06	3.33E-06	9.73E-04	3.75E-03	3.24E-02	1.85E-04	-1.85E-04
PHM	3.96E-04	1.58E-03	1.18E-02	-1.92E-05	1.92E-05	1.58E-03	5.69E-03	4.01E-02	2.59E-04	-2.59E-04
PDHM	2.65E-04	1.01E-03	1.05E-02	-2.78E-08	1.11E-07	9.43E-04	3.47E-03	3.40E-02	0.00E+00	0.00E+00
PRM	2.38E-04	1.02E-03	1.02E-02	-9.36E-06	9.44E-06	1.08E-03	4.15E-03	3.16E-02	2.06E-04	-1.68E-04
P-PPM	3.95E-04	1.57E-03	1.17E-02	-1.88E-05	1.88E-05	1.57E-03	5.67E-03	4.00E-02	2.56E-04	-2.56E-04
WENO23	2.96E-04	1.11E-03	1.02E-02	8.55E-06	-8.55E-06	1.04E-03	3.86E-03	3.21E-02	1.01E-04	-1.01E-04
WENO35	6.81E-05	3.08E-04	4.46E-03	0.00E+00	0.00E+00	4.17E-04	1.85E-03	2.93E-02	0.00E+00	0.00E+00
M-PPM	9.12E-05	4.17E-04	7.36E-03	0.00E+00	0.00E+00	5.25E-04	2.19E-03	2.70E-02	1.02E-04	-1.02E-04

Table V. Run times in seconds and percent deviation from PPM run time for the vortex test case interpolating from a  $1/3^\circ$  grid to a  $1/2.5^\circ$  grid.

Method	PPM	PHM	PDHM	PRM	P-PPM	M-PPM	WENO23	WENO35
Runtime (sec)	2.528	2.446	2.691	2.169	1.961	2.713	2.401	3.504
% deviation from PPM	-	-3.2%	+6.4%	-14.2%	-22.4%	+7.3%	-5.0%	+38.6%

5. Conclusions

An intercomparison of various subgrid-scale functional approximations has been performed in the context of conservative cascade interpolation on a latitude-longitude grid. Eight sets of test cases have been performed, interpolating four data profiles both from a  $T42$  grid to a  $2^\circ$  grid and from a  $2^\circ$  grid to a  $T42$  grid to measure the accuracy and oscillation properties of the functions. For all test cases, PDHM generally gives the best accuracy of the three-cell stencil methods. It seems unlikely that the economy of P-PPM would outweigh its comparative lack of accuracy compared with PDHM. WENO35 gives the best accuracy of the five-cell stencil methods, but requires the most computation. M-PPM seems to be a good alternative to WNEO35 with a large decrease in computational burden and a small relative decrease in accuracy.

Caution should be taken when using a non-oscillatory method, which is not strictly monotonic, to ensure that the orders of magnitude of monotonicity and positivity violation reported herein (of order 1%) are within acceptable bounds. A post-processing positive-definite filter may be employed to ensure that no negative values are produced in the interpolation for positive species. Note also that tunable parameters of the the non-oscillatory reconstructions M-PPM, WENO23, WENO35, PDHM, PHM and P-PPM may be tweaked for a particularly sensitive application until the oscillations are satisfactorily controlled for representative data. All subgrid reconstructions

in this study could be implemented in any conservative remapping algorithm employing 1-D sweeps, such as the conservative cascading implemented in cubed sphere geometry (Lauritzen and Nair, 2008).

Acknowledgements

The first author acknowledges funding support from the Department of Energy (DOE) Computational Science Graduate Fellowship (CSGF) program and from the Institute for Mathematics Applied to the Geosciences (IMAGe) at the National Centre for Atmospheric Research (NCAR). The first author also acknowledges the Graduate Student Visitor Program of NCAR's Advanced Study Program (ASP) for providing the setting for this research to occur. NCAR is supported by the National Science Foundation. The authors are grateful for the thorough comments given by reviewers and believe the manuscript is much improved as a result.

Appendix A

Here, the WENO23 method will be updated from the one defined in Kurganov and Levy (2000) for a non-uniform grid spacing. We define cell  $I_i$  to have grid spacing  $\Delta x_i$  defined within  $[x_{i-1/2}, x_{i+1/2}]$  with geometric centre  $x_i$ , cell mean  $\bar{u}_i$ . Following the notation of Kurganov and Levy (2000), we here define the three polynomials

$P_{i,L}(x)$ ,  $P_{i,R}(x)$  and  $P_{i,EXACT}(x)$  for an arbitrary cell of index  $i$ . Recall that  $P_{i,C}(x)$  is defined purely as a function of  $P_{i,L}$ ,  $P_{i,R}$  and  $P_{i,EXACT}$ . In a point-wise framework, polynomial reconstruction must match point values, but in the finite-volume framework, cell means must be replicated, requiring use of the polynomial's primitive. The primitive reconstruction principle of Harten *et al.* (1987), which is consistent with the finite volume formulation, gives the following three relations to constrain the coefficients of

$$P_{i,EXACT}(x) = s_{i,0} + s_{i,1}(x - x_i) + s_{i,2}(x - x_i)^2:$$

$$\int_{x_i - \Delta x_i/2}^{x_i - \Delta x_i/2 - \Delta x_{i-1}} P_{i,EXACT}(x) dx = \bar{u}_{i-1} \Delta x_{i-1},$$

$$\int_{x_i - \Delta x_i/2}^{x_i + \Delta x_i/2} P_{i,EXACT}(x) dx = \bar{u}_i \Delta x_i,$$

$$\int_{x_i + \Delta x_i/2}^{x_i + \Delta x_i/2 + \Delta x_{i+1}} P_{i,EXACT}(x) dx = \bar{u}_{i+1} \Delta x_{i+1}$$

Integration yields a system of equations of the form  $A\mathbf{s} = \mathbf{u}$ , where  $\mathbf{s} = [s_{i,0}, s_{i,1}, s_{i,2}]^T$  and  $\mathbf{u} = [\bar{u}_{i-1}, \bar{u}_i, \bar{u}_{i+1}]^T$ . Therefore, the coefficient vector,  $\mathbf{c}$ , is given by  $\mathbf{s} = A^{-1}\mathbf{u}$ . The matrix  $A$  is given by

$$A = \frac{1}{2} \begin{bmatrix} 2 & -\Delta x_i - \Delta x_{i-1} & \frac{1}{2} \Delta x_i^2 + \Delta x_i \Delta x_{i-1} + \frac{2}{3} \Delta x_{i-1}^2 \\ 2 & 0 & \frac{1}{6} \Delta x_i^2 \\ 2 & \Delta x_i + \Delta x_{i+1} & \frac{1}{2} \Delta x_i^2 + \Delta x_i \Delta x_{i+1} + \frac{2}{3} \Delta x_{i+1}^2 \end{bmatrix}.$$

In practice, this matrix inverse is precomputed and a matrix-vector multiply renders the coefficients during run time. The linear polynomials  $P_{i,L}(x) = l_{i,0} + l_{i,1}(x - x_i)$  and  $P_{i,R}(x) = r_{i,0} + r_{i,1}(x - x_i)$  are defined similarly but are simple enough to solve without a linear system. The coefficients are as follows:  $l_{i,0} = r_{i,0} = \bar{u}_i$ ,  $l_{i,1} = 2(\bar{u}_i - \bar{u}_{i-1}) / (\Delta x_i + \Delta x_{i-1})$  and  $r_{i,1} = 2(\bar{u}_{i+1} - \bar{u}_i) / (\Delta x_i + \Delta x_{i+1})$ .

The smoothness indicators must also be re-derived to account for non-uniform grid spacing, though the functional form is quite similar to that given in Kurganov and Levy (2000). They are as follows (using the same notation):

$$IS_{i,L} = l_{i,1}^2 \Delta x_i^2,$$

$$IS_{i,R} = r_{i,1}^2 \Delta x_i^2,$$

$$IS_{i,C} = c_{i,1}^2 \Delta x_i^2 + \frac{13}{3} c_{i,2}^2 \Delta x_i^4,$$

where  $c_{i,0}$ ,  $c_{i,1}$  and  $c_{i,2}$  are coefficients of  $P_{i,C}(x)$ .

**Appendix B**

Here, we describe the process of creating the polynomial used to obtain interface values for M-PPM in step 2 of

the summary. We have a five-cell stencil,  $I_{i-2}, \dots, I_{i+2}$ , centred on cell  $i$ . First, we calculate jump severity indicators,  $S_L$  and  $S_R$ , centred on cells  $I_{i-1}$  and  $I_{i+1}$  (respectively), using Equation (2). These will detect discontinuities on either cell boundary of cells  $I_{i-1}$  and  $I_{i+1}$ . If  $S_L \geq S^*$ , this indicates that there is a sufficiently severe discontinuity on either the left boundary (arising from cell  $I_{i-2}$ ) or the right boundary (arising from cell  $I_i$ ). If the discontinuity is on the left boundary, equation (3) does not take cell  $I_{i-2}$  into account, and thus the oscillation is not controlled. The same arguments apply for  $S_R$ .

If both  $S_L < S^*$  and  $S_R < S^*$ , then we compute a centred, fifth-order accurate, five-cell stencil polynomial on cells  $I_{i-2} \dots I_{i+2}$ , which is identical to  $\tilde{u}_{opt}(x)$  of Capdeville (2008). If  $S_L \geq S^*$ , then we neglect cell  $I_{i-2}$  to get rid of the potential discontinuity, computing a right-biased, fourth-order accurate, four-cell stencil polynomial,  $P_{i,R4}(x)$ , from cells  $I_{i-1} \dots I_{i+2}$ . Likewise, if  $S_R \geq S^*$ , we neglect cell  $I_{i+2}$ , computing a left-biased, fourth-order accurate, four-cell stencil polynomial,  $P_{i,L4}(x)$ , from cells  $I_{i-2} \dots I_{i+1}$ . If both  $S_L \geq S^*$  and  $S_R \geq S^*$ , a centred, third-order accurate, three-cell stencil polynomial (identical to  $P_{i,EXACT}(x)$  from Appendix A) is computed using cell  $I_{i-1} \dots I_{i+1}$ . We use the primitive reconstruction principle of Harten *et al.* (1987) to constrain the polynomial coefficients on the fourth-order accurate polynomials as follows.

$$\int_{x_i - \Delta x_i/2 - \Delta x_{i-1}}^{x_i - \Delta x_i/2 - \Delta x_{i-1} - \Delta x_{i-2}} P_{i,L4}(x) dx = \bar{u}_{i-2} \Delta x_{i-2},$$

$$\int_{x_i - \Delta x_i/2}^{x_i - \Delta x_i/2} P_{i,L4}(x) dx = \bar{u}_{i-1} \Delta x_{i-1},$$

$$\int_{x_i - \Delta x_i/2 - \Delta x_{i-1}}^{x_i + \Delta x_i/2} P_{i,L4}(x) dx = \bar{u}_i \Delta x_i,$$

$$\int_{x_i + \Delta x_i/2}^{x_i + \Delta x_i/2 + \Delta x_{i+1}} P_{i,L4}(x) dx = \bar{u}_{i+1} \Delta x_{i+1},$$

$$\int_{x_i - \Delta x_i/2}^{x_i - \Delta x_i/2} P_{i,R4}(x) dx = \bar{u}_{i-1} \Delta x_{i-1},$$

$$\int_{x_i + \Delta x_i/2}^{x_i + \Delta x_i/2} P_{i,R4}(x) dx = \bar{u}_i \Delta x_i,$$

$$\int_{x_i + \Delta x_i/2}^{x_i + \Delta x_i/2 + \Delta x_{i+1}} P_{i,R4}(x) dx = \bar{u}_{i+1} \Delta x_{i+1},$$

$$\int_{x_i + \Delta x_i/2}^{x_i + \Delta x_i/2 + \Delta x_{i+1} + \Delta x_{i+2}} P_{i,R4}(x) dx = \bar{u}_{i+2} \Delta x_{i+2}.$$

These constraints form a linear system just as in Appendix A. However, the matrix is too large to give explicitly here. In practice, this matrix is inverted analytically for accuracy purposes using a program capable of symbolic algebraic manipulation, and it is precomputed so that a matrix–vector multiply renders the polynomial. As can be seen, the polynomial that renders the interface values for M-PPM will be from third-order to fifth-order accurate. Because classical PPM is formally fourth-order accurate when integrated and applied to smooth data and a uniform mesh, it makes sense to try to keep the interface values to fourth-order accuracy or more. We note that the case where the interface values are limited to third-order accuracy, which is necessary to ensure bounded oscillations, does not occur often in any of our test cases.

## References

- Amat S, Busquier S, Candela V. 2003. A polynomial approach to the piecewise hyperbolic methods. *Int. J. Comput. Fluid Dyn.* **17**: 205–217.
- Artebrant R, Schroll JH. 2006. Limiter-free third order logarithmic reconstruction. *SIAM J. Sci. Comput.* **28**: 359–381.
- Blossey PN, Durran DR. 2008. Selective monotonicity preservation in scalar advection. *J. Comput. Phys.* **227**: 5160–5183.
- Capdeville G. 2008. A central WENO scheme for solving hyperbolic conservation laws on non-uniform meshes. *J. Comput. Phys.* **227**: 2977–3014.
- Colella P, Sekora MD. 2008. A limiter for PPM that preserves accuracy at smooth extrema. *J. Comput. Phys.* **227**: 7069–7076.
- Colella P, Woodward PR. 1984. The Piecewise Parabolic Method (PPM) for gas-dynamical simulations. *J. Comput. Phys.* **54**: 174–201.
- Harten A, Engquist B, Osher S, Chakravarthy SR. 1987. Uniformly high order accurate essentially non-oscillatory schemes, III. *J. Comput. Phys.* **71**: 231–303.
- Jones PW. 1999. First- and second-order conservative remapping schemes for grids in spherical coordinates. *Mon. Weather Rev.* **127**: 2204–2210.
- Kurganov A, Levy D. 2000. A third-order semidiscrete central scheme for conservation laws and convection-diffusion equations. *SIAM J. Sci. Comput.* **22**: 1461–1488.
- Lauritzen PH, Nair RD. 2008. Monotone and conservative cascade remapping between spherical grids (CaRS): Regular latitude–longitude and cubed-sphere grids. *Mon. Weather Rev.* **136**: 1416–1432.
- Liu XD, Osher S, Chan T. 1994. Weighted essentially non-oscillatory schemes. *J. Comput. Phys.* **115**: 200–212.
- Marquina A. 1994. Local piecewise hyperbolic reconstruction of numerical fluxes for nonlinear scalar conservation laws. *SIAM J. Sci. Comput.* **15**: 892–915.
- Nair RD, Cote J, Staniforth A. 1999. Monotonic cascade interpolation for semi-Lagrangian advection. *Q. J. R. Meteorol. Soc.* **125**: 197–212.
- Nair RD, Machenhauer B. 2002. The mass-conserving cell-integrated semi-Lagrangian advection scheme on the sphere. *Mon. Weather Rev.* **130**: 649–667.
- Nair RD, Scroggs JS, Semazzi FHM. 2002. Efficient conservative global transport schemes for climate and atmospheric chemistry models. *Mon. Weather Rev.* **130**: 2059–2073.
- Nair RD, Scroggs JS, Semazzi FHM. 2003. A forward-trajectory global semi-Lagrangian transport scheme. *J. Comput. Phys.* **190**: 275–294.
- Norman MR, Nair RD. 2008. Inherently conservative non-polynomial based remapping schemes: Application to semi-Lagrangian transport. *Mon. Weather Rev.* **136**: 5044–5061.
- Purser RJ, Leslie LM. 1991. An efficient interpolation procedure for high-order three-dimensional semi-Lagrangian models. *Mon. Weather Rev.* **119**: 2492–2498.
- Serna S. 2006. A class of extended limiters applied to piecewise hyperbolic methods. *SIAM J. Sci. Comput.* **28**: 123–140.
- Serna S, Marquina A. 2004. Power ENO methods: a fifth-order accurate weighted power eno method. *J. Comput. Phys.* **194**: 632–658.
- Shu CW. 1999. High order ENO and WENO schemes for computational fluid dynamics. In: *High-Order Methods for Computational Physics, Lecture Notes in Computational Science and Engineering*, vol. 9, Barth TJ, Deconinck H (eds). Springer: Heidelberg, Germany; pp 439–582.
- Shu CW, Osher S. 1988. Efficient implementation of essentially non-oscillatory shock-capturing schemes. *J. Comput. Phys.* **72**: 439–471.
- Ulrich PA, Lauritzen PH, Jablonowski C. 2009. Geometrically Exact Conservative Remapping (GECORe): Regular latitude–longitude and cubed-sphere grids. *Mon. Weather Rev.* In press.
- Xiao F, Yabe T, Peng X, Kobayashi H. 2002. Conservative and oscillation-less atmospheric transport schemes based on rational functions. *J. Geophys. Res. (Atmospheres)* **107**: 2.1–2.11.
- Zalesak ST. 1979. Fully multidimensional flux-corrected transport algorithms for fluids. *J. Comput. Phys.* **31**: 335–362.
- Zerroukat M, Wood N, Staniforth A. 2004. SLICE-S: A semi-Lagrangian inherently conserving and efficient scheme for transport problems on the sphere. *Q. J. R. Meteorol. Soc.* **130**: 2649–2664.
- Zerroukat M, Wood N, Staniforth A. 2005. A monotonic and positive-definite filter for a semi-Lagrangian inherently conservative and efficient (SLICE) scheme. *Q. J. R. Meteorol. Soc.* **131**: 2923–2936.
- Zerroukat M, Wood N, Staniforth A. 2006. The Parabolic Spline Method (PSM) for conservative transport problems. *Int. J. Numer. Methods* **51**: 1297–1318.